

# STELLAR: Scaling 3D Perception Large Models for Autonomous Driving

Yingwei Li<sup>\*1</sup> Xin Huang<sup>\*1</sup> Yang Liu<sup>\*1</sup> Yang Fu<sup>1,2</sup> Alex Zihao Zhu<sup>1</sup> Chen Song<sup>1</sup> Junwen Yao<sup>1</sup>  
 Anant Subramanian<sup>1</sup> Hao Xiang<sup>1</sup> Weijing Shi<sup>1</sup> Yuliang Zou<sup>1</sup> Tom Hoddes<sup>1</sup> Zhaoqi Leng<sup>1</sup> Govind Thattai<sup>1</sup>  
 Dragomir Anguelov<sup>1</sup> Mingxing Tan<sup>1</sup>

## Abstract

Model scaling has demonstrated remarkable success through large-scale training on diverse datasets. It remains an open question whether the same paradigm would apply to autonomous driving perception systems due to unique challenges, such as fusing heterogeneous sensor data and the need for sophisticated 3D spatial understanding. To bridge this gap, we present a comprehensive study on systematically analyzing the impact of scale on these systems. We develop our STELLAR model based on Sparse Window Transformer, by extending the input modalities to include LiDAR, radar, camera, and map prior. We train the model on a large-scale dataset of 50 million driving examples with up to 500 million parameters. Our large-scale experiments reveal empirical scaling trends that connect model performance to model size, data, and compute. The resulting model establishes a new state-of-the-art on the Waymo Open Dataset challenge, outperforming prior arts by a large margin. Our work demonstrates that large-scale training is a highly promising path for advancing the capabilities of perception models for autonomous driving.

## 1. Introduction

Perception is a fundamental task for autonomous driving, responsible for interpreting the surrounding environment using data from sensors such as cameras, LiDAR, and radar. Recent breakthroughs have significantly enhanced these perception models, leading to more accurate 3D bounding box detection (Zhang et al., 2023; 2024; Huang et al., 2025a; Agro et al., 2025) and a comprehensive understanding of the scene through segmentation (Wu et al., 2024; Sun et al., 2024). These enhanced capabilities are foundational to

<sup>\*</sup>Equal contribution <sup>1</sup>Waymo, Mountain View, CA, USA  
<sup>2</sup>UCSD, La Jolla, CA, USA. Correspondence to: Yingwei Li <ywli@waymo.com>, Xin Huang <xchuang@waymo.com>, Mingxing Tan <tanmingxing@waymo.com>.

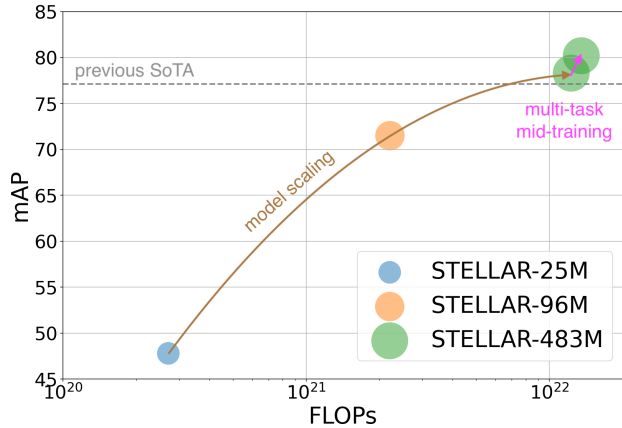


Figure 1. STELLAR achieves better 3D detection performance through scaling model parameters and multi-task mid-training on high quality driving data, measured by average L2 APH on the Waymo Open Dataset validation set. The dashed horizontal line represents previous state-of-the-art using up to 4 temporal frames.

enabling safer and more robust driving in complex environments (Schreier et al., 2023; Hu et al., 2023).

Recently, large foundation models have represented a significant paradigm shift in artificial intelligence, driven by the principle of training at an unprecedented scale. By dramatically increasing model parameters and leveraging vast, internet-scale datasets, these models have achieved state-of-the-art performance and unlocked emergent capabilities across both language (Brown et al., 2020; Kaplan et al., 2020; Hoffmann et al., 2022) and vision (Achiam et al., 2023; Team et al., 2023) domains.

It remains an open question whether these scaling paradigms apply to 3D perception for autonomous driving, due to several unique and formidable challenges. First, unlike existing foundation models that process language text or image inputs, driving models typically ingest and fuse heterogeneous data from multiple sensors, combining multi-modal features from LiDAR point clouds, multi-view camera images, radar images, and map prior. Developing architectures to effectively account for multi-modal sensor fusion is crucial to model scaling. Second, processing these dense, high-resolution sensor inputs over long ranges imposes sig-

nificant computational challenges as model size increases. Third, driving perception demands a sophisticated 3D spatial understanding of the world. This requirement for precise geometric prediction within dynamic environments distinguishes it from general-purpose foundation models, which predominantly operate on 2D images or textual data. Finally, the training paradigms differ significantly. While language models leverage self-supervised learning on unlabeled data, perception models typically rely on high-quality, manually-annotated labels. This costly process creates a major bottleneck for data scaling.

In this paper, we present a comprehensive study on scaling a multi-modal perception Transformer model for autonomous driving across both model and data, as shown in Fig. 1. Our main contributions are threefold:

- We develop a scalable STELLAR model that jointly process multimodal data, from LiDAR, radar, and camera sensors, using a unified sparse window Transformer backbone (Sun et al., 2022).
- We scale up our models up to 500 million parameters and train them with 50 million examples from our proprietary driving logs. Both the model size and data size are orders of magnitude larger than prior art. We identify and characterize the underlying scaling properties that uncover performance gains related to model size, data volume, and compute.
- Our best STELLAR model establishes a new state-of-the-art on the competitive Waymo Open Dataset, outperforming prior arts by a large margin.

## 2. Related Work

### 2.1. Perception for Autonomous Driving

Perception is a fundamental capability for autonomous systems, responsible for processing raw sensor inputs to interpret the driving environment. Substantial progress has advanced performance across diverse perception tasks, including 3D object detection (Zhang et al., 2023; 2024; Huang et al., 2025a; Agro et al., 2025), segmentation (Wu et al., 2024; Sun et al., 2024), and occupancy prediction (Wei et al., 2023; Tian et al., 2023).

Despite these successes, it remains unclear how effectively autonomous driving perception models scale with increased data and model size. This gap persists largely due to the significant challenges of scaling architectures that process dense multi-modal inputs, alongside the prohibitive cost of collecting and labeling driving data at a massive scale. To address this uncertainty, our work provides a comprehensive empirical study of scaling for perception, specifically 3D detection, in autonomous driving. We train models ranging

up to 500 million parameters on a dataset of over 50 million driving examples.

### 2.2. 3D Object Detection

3D object detection serves as one of the most critical perception tasks in autonomous driving, with modern approaches including LiDAR and camera-based paradigms. LiDAR detectors (Zhou & Tuzel, 2018; Sun et al., 2022; Zhang et al., 2024; Huang et al., 2025a) have achieved dominant performance by leveraging sparse voxelization and efficient backbone architectures. Concurrently, camera-based detection has undergone a pivotal shift from perspective-view to bird’s-eye-view (BEV) representations (Phillion & Fidler, 2020; Huang et al., 2021; Li et al., 2024). To enable better scalability, our approach synthesizes these paradigms: we extend the sparse, voxel-based SWFormer backbone (Sun et al., 2022) to integrate camera features, by projecting camera features into a unified BEV space following (Phillion & Fidler, 2020).

### 2.3. Foundation Models for Autonomous Driving

Foundation models trained on web-scale data have established a significant paradigm shift in artificial intelligence, achieving state-of-the-art results across language (Radford et al., 2018; Devlin et al., 2019) and vision domains (Radford et al., 2021; Caron et al., 2021). These breakthroughs are underpinned by established scaling properties (Kaplan et al., 2020; Hoffmann et al., 2022) that quantify the relationship between model size, dataset volume, and performance.

Within autonomous driving, self-supervised learning has emerged as a dominant strategy for leveraging vast amount of unlabeled LiDAR data. Early work (Hess et al., 2023) demonstrates that geometric reconstruction tasks can yield robust features without manual labels. Subsequent research has introduced more complex representations, utilizing unsupervised occupancy fields (Agro et al., 2024) and 3D volumetric rendering (Yang et al., 2024) as supervision signals. More recent paradigms (Ljungbergh et al., 2025; Wozniak et al., 2025) further unify geometric and semantic signals to improve representations for downstream perception tasks.

While these paradigms primarily focus on the design of proxy tasks to learn from unlabeled data, STELLAR investigates a different axis: the impact of scaling auto-labeled and supervised data on 3D perception. While prior work has successfully verified scaling laws for behavior prediction and planning models (Huang et al., 2025b; Baniodeh et al., 2025), these systems typically operate on sparse inputs (e.g., map coordinates and trajectories). Scaling perception models, however, presents a distinct and greater computational challenge. This difficulty stems from processing dense, high-dimensional sensor inputs like camera data and massive LiDAR point clouds, leaving perception scalability

Statistics	Ours	Prior Work
Run segments	59M	1M(Yaak, 2025)
Hours of driving	169K	5K(Yaak, 2025)
Camera images	47.2B	2.7M(Wilson et al., 2023)
LiDAR frames	6B	6M(Wilson et al., 2023)
3D bounding boxes	431B	5B(Karnchanachari et al., 2024)

Table 1. We train STELLAR on a large-scale 3D perception driving dataset, which includes multi-modal input features at a scale exceeding existing literature.

an open question due to the challenges of scaling raw data inputs and their corresponding training targets.

In this work, we address this gap by presenting the first empirical scaling study for autonomous driving perception. We establish this study by training a transformer-based, multi-modal model while scaling both its parameters and the training dataset to an unprecedented scale.

### 3. Data

We introduce a large-scale driving dataset designed to study the scaling properties of perception models in autonomous driving. Collected from millions of miles of high-quality human and autonomous driving demonstrations, the dataset captures extensive spatiotemporal diversity. It spans more than 10 U.S. cities, covering urban, suburban, freeway, and indoor (e.g., parking garage) environments across various times of day and adverse weather conditions.

The dataset comprises over 50M training examples. Each example is derived from a unique 10-second driving segment discretized at 10Hz, consistent with standard benchmarks such as Waymo Open (Sun et al., 2020) and nuScenes (Cesar et al., 2020). The sensor suite features multi-modal data including LiDAR, camera, and radar. Additionally, we follow (Pfister et al., 2000; Yang et al., 2020) to construct a surfel map prior by estimating mean coordinates, surface normals, and color from aligned LiDAR points and camera pixels. To construct a single training example from the 100 frames available in each segment, we randomly sample 4 frames (1 current and 3 historical). Key statistics and comparisons to prior work are detailed in Tab. 1.

For supervision, our dataset provides 7-DoF (center<sub>x</sub>, center<sub>y</sub>, center<sub>z</sub>, length, width, height, heading) 3D bounding box labels for multiple object categories, comprising both manual annotations and auto-generated pseudo-labels. Due to the complexity of manual annotation at scale, we employ an off-board autolabeler based on (Li et al., 2023b). This model, which leverages long-term temporal information (past and future frames) and takes multi-modality sensor data as inputs, was trained on our high-quality, manually-annotated subset. The trained autolabeler was then used to generate pseudo-labels for the remainder of our dataset.

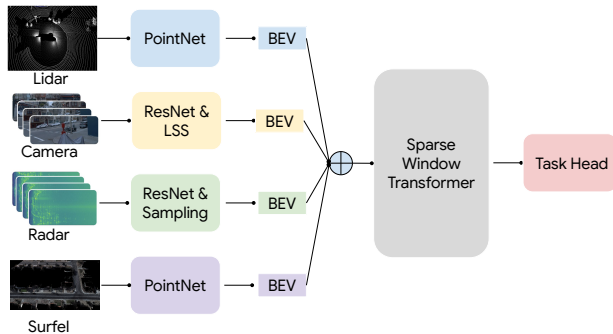


Figure 2. Overview of STELLAR, a multi-modal perception model. The model projects LiDAR, radar, and surfel inputs directly into a bird’s-eye-view (BEV) representation, while camera features are mapped to BEV via a lift-splat-shoot (LSS) transformation. These features are subsequently concatenated and processed by a sparse window transformer backbone. Task-specific heads are applied to the unified BEV features to produce the final outputs.

## 4. STELLAR

We present STELLAR, a simple and scalable perception model designed to operate across multiple dimensions: input modalities, temporal context, perception tasks, model size, and perception ranges. The high-level model architecture is shown in Fig. 2. The remainder of this section will elaborate on how STELLAR achieves scalability across dimensions.

### 4.1. Multi-Modal and Multi-Frame Sensor Inputs

Our model takes four modalities: LiDAR point cloud, camera images, radar polar images, and surfel map prior, as described in Sec. 3. We use modality specific encoders to construct bird’s-eye-view feature maps. The LiDAR encoder, following (Sun et al., 2022), uses dynamic voxelization (Zhou et al., 2020) and a PointNet-style embedding model (Qi et al., 2017; Lang et al., 2019) to generate sparse voxel features. We introduce an extra projection layer to align LiDAR features with camera and radar modalities. For camera images, a ResNet (He et al., 2016) and a lift-splat-shoot (LSS) module (Phillion & Fidler, 2020) are used to produce dense image features in bird’s-eye-view (BEV). A separate ResNet is employed to encode radar polar images, and their resulting feature maps are resampled into Cartesian coordinates. The surfel map prior shares the same format as LiDAR points, and is then fed into a surfel encoder with the same architecture of the LiDAR encoder (Fu et al., 2026). These encoded features are then fused into a unified BEV feature map through concatenation, similar to BevFusion (Liu et al., 2023), as shown in Fig. 2.

To further enhance capability, we aggregate LiDAR features over a temporal window following (Luo et al., 2018), which allows the model to reconstruct geometries of partially occluded objects from varying viewpoints and utilize temporal cues to refine object heading estimation.

## 4.2. Perception Tasks

The BEV features are fed into a multi-scale SWFormer (Sun et al., 2022) backbone that consists of a multi-scale feature extractor and a multi-scale feature fuser. The backbone’s output is then passed to three distinct heads for 3D detection, occupancy prediction, and roadgraph prediction tasks.

The 3D detection head extends SWFormer’s approach, performing detection in two stages. First, it refines foreground and background voxels via segmentation and voxel diffusion. Second, a CenterNet-style (Duan et al., 2019) detection head produces the final classification and box regression outputs.

The occupancy head and roadgraph head each employ a series of convolutional layers to refine backbone features and subsequently produce per-voxel logits. For occupancy prediction, these logits are passed to an MLP to generate a per-voxel semantic classification. In contrast, for roadgraph prediction, the logits are used to predict predefined geometric targets, such as lanes and road boundaries.

## 4.3. Scalable Model Size

Although the model processes different modalities and performs various tasks, the computational load is primarily concentrated in the transformer backbone. For instance, in our largest model, the backbone accounts for over 90% of the total parameters. This centralized architectural design simplifies the scaling process and requires less hyperparameter tuning. To implement this, we scale the model size by increasing both its width (hidden dimension size, feed-forward ratio) and depth (number of layers), following existing scaling literature (Kaplan et al., 2020; Hoffmann et al., 2022; Petty et al., 2024).

## 4.4. Scalable Perception Range

In practical applications, perception models must support different perception ranges depending on the operational scenario. For example, freeway driving typically requires a larger perception range than driving on surface streets. By virtue of its transformer-style architecture and sparse representation, our model supports training at one range and inference at a different range without requiring any changes to the model weights. While this paper follows the SWFormer (Sun et al., 2022) range settings for the Waymo Open Dataset, our design is inherently scalable to larger or smaller ranges as dictated by specific requirements.

## 4.5. Scaling Down with Distillation

We also study the process of distillation, which can improve the accuracy of smaller and cheaper model variants using the scaled up STELLAR models as teachers. This approach leverages teacher predictions directly from raw CenterNet

heatmaps as training targets for the student heatmaps. We utilize the standard CenterNet loss framework, specifically adapting the focal loss to accommodate continuous targets.

## 5. Training Recipe

We employ a three-stage training strategy for STELLAR: the model is initially pre-trained on the 50 million pre-training dataset (Sec. 3), subsequently trained on 600K human-annotated segments, and finally fine-tuned on 798 WOD segments.

During pre-training, we employ the LAMB optimizer (You et al., 2019) with a constant learning rate of  $1e^{-2}$  and a global batch size of 1024. Following (He et al., 2019; Ibrahim et al., 2024; Hägele et al., 2024), we utilize a constant learning rate schedule to enable evaluation and mid-training at various checkpoints without the need for retraining. Training proceeds for up to 50K steps, approximately equivalent to one epoch over the dataset. To minimize training on temporally correlated frames and maximize data diversity, we sample our batches by selecting one random frame plus three history frames per driving segment. We supervise solely on positive, high-confidence auto-labels (i.e., confidence score  $\geq 0.3$ ). We set the DropPath ratio (Huang et al., 2016) to 0.5 and weight decay to  $1e^{-3}$ . For simplicity, we focus exclusively on the 3D detection task and utilize standard LiDAR, camera, and radar inputs, due to the complexity of generating surfel inputs at this scale.

During mid-training, we retain the same optimizer but adopt a cosine decay learning rate schedule, starting with an initial learning rate of  $1e^{-4}$ . We train for 20K steps with a batch size of 256. In this phase, we introduce additional internal dense tasks, such as occupancy prediction and roadgraph prediction, and incorporate surfels as an extra input modality generated from LiDAR and camera inputs, as described in Sec. 3.

Finally, we finetuned on the WOD training set for the 3D detection task, using a cosine decay learning rate schedule with an initial learning rate of  $3e^{-5}$ . We train for 10K steps with a global batch size of 256. We applied data augmentation as described in (Sun et al., 2022).

## 6. Scaling

This section outlines scaling methodology and reports empirical results during pre-training. We scale towards 500M parameters and 50M driving examples, representing a cumulative computational budget exceeding 10 ZettaFLOPs.

Notably, to address high device memory pressure from model scaling, we employed gradient checkpointing (Chen et al., 2016; Bulatov, 2018), which discards intermediate activations within PointNet and SWFormer during the forward

Model Size	Width	Feed-forward Ratio	Layers
25M	128	2	[2, 3, 2, 3, 2]
96M	256	8	[4, 6, 4, 6, 4]
251M	384	10	[5, 7, 5, 7, 5]
364M	384	15	[5, 8, 5, 8, 5]
483M	384	18	[6, 9, 6, 9, 6]

Table 2. Overview of STELLAR configurations at different sizes, by modifying key parameters in the Sparse Window Transformer.

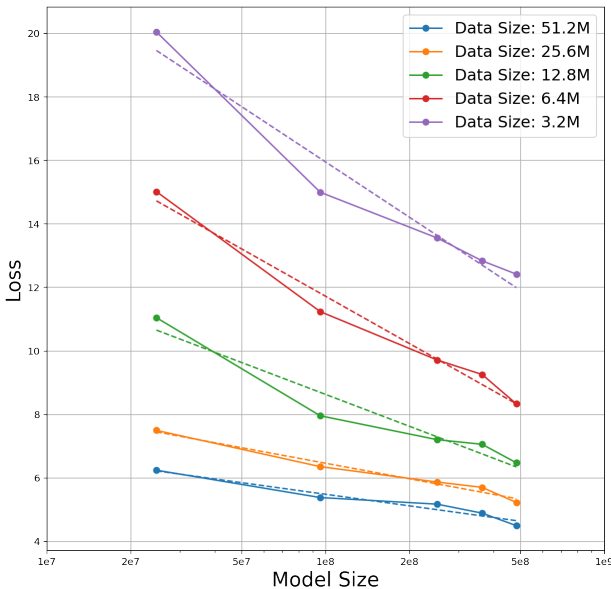


Figure 3. Model scaling curves. Final loss consistently decreases as model parameter size increases. Log-linear fits are overlaid for each dataset size to illustrate the scaling trend.

pass and recomputes them for backpropagation.

### 6.1. Model Scaling

We first scale STELLAR at different model sizes, by varying the transformer parameters, including hidden dimension size, feed-forward ratio, and number of layers, as shown in Tab. 2.

Figure 3 illustrates model performance as a function of parameter count across varying dataset sizes. We observe two trends. First, for any fixed dataset size, increasing the model’s parameter count consistently reduces the final loss. Second, the magnitude of this gain from model scaling is highly dependent on the dataset size. The loss curves are steepest for smaller datasets (e.g., 3.2M examples) and become progressively flatter as the dataset size increases (e.g., 51.2M examples).

We add a log-linear fit for each curve in dashed lines. Unlike the strong, log-linear scaling laws commonly observed in LLM literature, our observed scaling trend exhibits di-

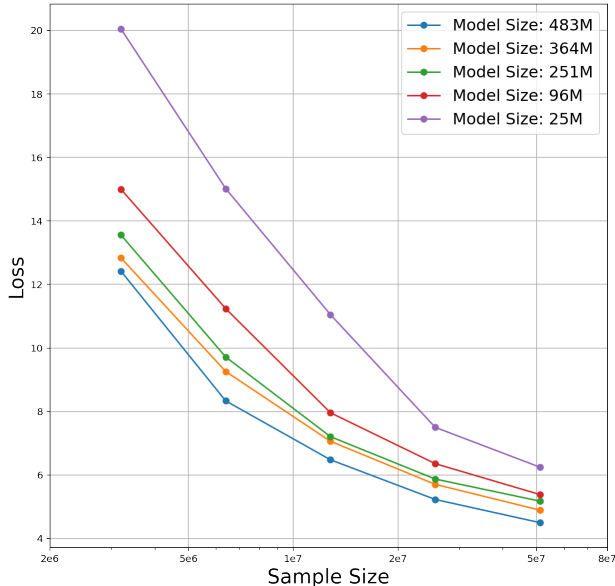


Figure 4. Data scaling curves. Increasing the training example size consistently reduces the final loss for all model sizes.

minishing returns. We attribute this to two factors. First, our model is a complex, multi-component architecture (e.g., with various encoders), not a single, homogeneous transformer decoder. Second, we primarily scale the transformer backbone while other components remain fixed. This fixed-size parameter overhead distorts the scaling curve and masks the true scaling behavior of the transformer component.

### 6.2. Data Scaling

Fig. 4 illustrates the impact of data scaling on models of varying sizes. We observe a consistent trend that increasing the training example size monotonically reduces the loss for all models, though this benefit exhibits diminishing returns as the loss curves flatten.

Similar to our model scaling findings, we do not observe the strong log-linear scaling laws often reported in LLM literature. We attribute this to data quality being bounded by the qualities of auto-labels and the intrinsic redundancy of driving data, even across distinct segments. We leave further investigation of these factors to future research.

### 6.3. Compute Scaling

Fig. 5 illustrates the relationship between the total compute, measured in FLOPs (Floating-Point Operations), and the loss. Similar to Fig. 3, each colored line represents a model trained on a fixed dataset size. The trend indicates that as the FLOP budget increases, the model performance improves (i.e., loss decreases), which is consistent with our previous model and data scaling results.

Method	Overall L1		Overall L2		Vehicle L1		Vehicle L2		Pedestrian L1		Pedestrian L2		Cyclist L1		Cyclist L2	
	AP	APH	AP	APH	AP	APH	AP	APH	AP	APH	AP	APH	AP	APH	AP	APH
PointPillars (Lang et al., 2019)	69.0	63.5	62.8	57.8	72.1	71.5	63.6	63.1	70.6	56.7	62.8	50.3	64.4	62.3	61.9	59.9
SST (Fan et al., 2022a)	74.5	71.0	67.8	64.6	74.2	73.8	65.5	65.1	78.7	69.6	70.0	61.7	70.7	69.6	68.0	66.9
CenterFormer (Zhou et al., 2022)	75.6	73.2	71.4	69.1	75.0	74.4	69.9	69.4	78.0	72.4	73.1	67.7	73.8	72.7	71.3	70.2
SWFormer (Sun et al., 2022)	-	-	-	-	77.8	77.3	69.2	68.8	80.9	72.7	72.5	64.9	-	-	-	-
CenterPoint (Yin et al., 2021)	77.5	75.8	71.7	70.1	76.4	75.9	68.7	68.2	79.2	75.6	71.9	68.5	76.8	75.9	74.4	73.5
FSDv1 (Fan et al., 2022b)	79.6	77.4	72.9	70.8	79.2	78.8	70.5	70.1	82.6	77.3	73.9	69.1	77.1	76.0	74.4	73.3
FSDv2 (Fan et al., 2024)	81.8	79.5	75.6	73.5	79.8	79.3	71.4	71.0	84.8	79.7	77.4	72.5	80.7	79.6	77.9	76.8
HEDNet 4f (Zhang et al., 2023)	83.6	82.3	78.1	76.8	82.4	81.9	75.1	74.6	86.3	83.6	79.4	76.8	82.2	81.4	79.9	79.1
SAFDNet 4f (Zhang et al., 2024)	83.9	82.6	78.4	77.1	82.8	82.3	75.4	74.9	86.8	84.2	80.1	77.5	82.0	81.1	79.6	78.8
<b>STELLAR</b>	<b>86.7</b> (+2.8)	<b>85.3</b> (+2.7)	<b>81.6</b> (+3.2)	<b>80.2</b> (+3.1)	<b>84.3</b> (+1.5)	<b>83.9</b> (+1.6)	<b>77.1</b> (+1.7)	<b>76.7</b> (+1.8)	<b>87.5</b> (+0.7)	<b>84.7</b> (+0.5)	<b>81.4</b> (+1.3)	<b>78.6</b> (+1.1)	<b>88.2</b> (+6.0)	<b>87.2</b> (+5.9)	<b>86.3</b> (+6.4)	<b>85.4</b> (+6.3)

Table 3. Detailed performance comparison on the WOD validation set. We report Average Precision (AP) and Average Precision with Heading (APH) across three agent types at two difficulty levels (L1 and L2). Our method consistently achieves better results across all categories. Baselines include comparable methods that use up to 4 temporal frames. Best results are in **bold**, annotated with improvements over the runner-up. The ranking metric is underlined.

Method	History Frames	Overall L1		Overall L2	
		AP	APH	AP	APH
HEDNet (Zhang et al., 2023)	0	82.2	80.2	76.9	75.0
HEDNet (Zhang et al., 2023)	0	82.2	80.2	76.9	75.0
CenterFormer (Zhou et al., 2022)	15	82.3	80.9	77.6	76.3
BEVFusion (Liu et al., 2023)	2	82.7	81.4	77.7	76.3
MSF (He et al., 2023)	3	83.5	82.1	78.4	77.1
FSD++ (Fan et al., 2023)	6	83.5	82.1	78.4	77.1
LoGoNet (Li et al., 2023a)	4	83.1	81.8	78.4	77.1
SEED-L (Liu et al., 2024b)	2	83.5	82.1	78.7	77.3
LION (Liu et al., 2024a)	2	83.7	82.4	78.7	77.4
VADet (Huang et al., 2025a)	15	84.1	82.8	79.4	78.2
MAD (Agro et al., 2025)	99	86.0	84.3	81.8	80.2
<b>STELLAR</b>	<b>3</b>	<b>87.5</b> (+1.5)	<b>86.2</b> (+1.9)	<b>83.1</b> (+1.3)	<b>81.8</b> (+1.6)

Table 4. Overall performance comparison on the WOD test set. We report the average of Average Precision (AP) and Average Precision with Heading (APH), at two difficulty levels (L1 and L2). Our method achieves state-of-the-art performance using a total of 4 frames (including 3 history frames). Best results are in **bold**, annotated with improvements over the runner-up. The ranking metric is underlined.

We further visualize the “efficient frontier,” which represents the optimal model performance achievable for a given FLOPs budget. This frontier is dominated by the bottom-most curve (representing the largest dataset). This empirically demonstrates that the most effective way to utilize a given compute budget is to employ the largest possible dataset. On the other hand, using a large model on a small dataset (e.g., the rightmost point on the purple line) is highly compute-inefficient, yielding a significantly higher loss compared to what the same compute budget could achieve by using more data.

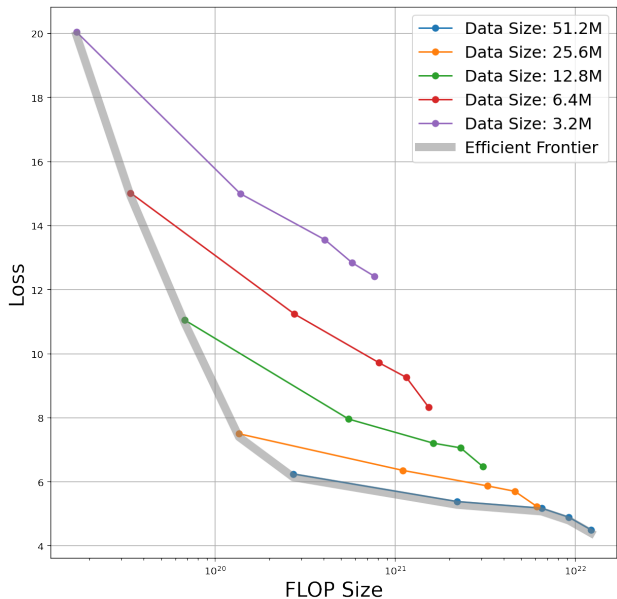


Figure 5. Compute scaling curves. Each dot represents a model size, and each line represents various model sizes training with a given data size. Both large models and larger datasets lead to lower loss. The efficient frontier curve indicates that for a fixed compute FLOPs budget, it is more effective to train a smaller model on a larger dataset than to train a larger model on a small dataset.

## 7. Evaluation

We evaluate the largest STELLAR (STELLAR-483M) on the Waymo Open Dataset (WOD) (Sun et al., 2020), following the mid-training and finetuning methodology described in Sec. 5. This benchmark consists of over a thousand 20-second scenes containing high-quality LiDAR and camera data from diverse geographies, including approximately 158K training frames and 40K validation frames. The dataset focuses on three major object categories: vehicle, pedestrian, and cyclist. To bridge the domain gap between WOD and our internal data, we finetune our mod-

Pre-training	Training Stage		L2 APH Overall
	Mid-training	Finetuning	
		✓ (From Scratch)	66.8
✓		✓	71.5
✓	✓	✓	75.7

Table 5. Ablation study on training recipe using STELLAR-96M model. Adding large-scale pre-training and high-quality mid-training stages significantly improves 3D detection in WOD.

els on the WOD training set before evaluating them on the validation and test sets.

### 7.1. Quantitative Results

Tab. 3 summarizes our results on the WOD validation set. These results demonstrate that STELLAR outperforms prior methods using only causal information (i.e., no future frames) up to 4 frames across all metrics. Notably, it boosts cyclist detection performance by a large margin.

Tab. 4 presents a comparison of STELLAR on the WOD test set against published methods on the leaderboard. We exclude methods that utilize ensembles, future frames, or test-time augmentation. Our results demonstrate that STELLAR sets a new state-of-the-art in this category. We attribute this success to the benefits of large-scale pre-training, which allows our model to achieve superior performance using significantly fewer temporal frames than complex memory-augmented approaches such as (Agro et al., 2025). Furthermore, our method is orthogonal to these memory-augmented strategies, and integrating STELLAR with such techniques holds strong promise for achieving even greater performance gains in future work.

### 7.2. Ablation

We validate the effectiveness of STELLAR through detailed ablation studies on training recipe, model scaling, mid-training tasks, multi-modal inputs, and temporal context. Unless otherwise specified, these ablations utilize the STELLAR-96M model and are evaluated on a subset of the WOD validation set for computational efficiency.

#### 7.2.1. TRAINING RECIPE

We first conduct ablations for our training recipe using the STELLAR-96M model. As shown in Tab. 5, the first row establishes a baseline, showing performance when training directly on WOD without pre-training or mid-training. Subsequent rows add each stage incrementally. Results indicate that detection performance improves significantly with the addition of pre-training on large-scale auto-labeled data and mid-training on high-quality human-labeled data.

Model Parameters	Overall	L2 APH		
		Vehicle	Pedestrian	Cyclist
25M	47.8	52.8	46.2	44.5
96M	71.5	76.3	66.8	71.6
483M	78.3	81.7	75.1	78.2

Table 6. Ablation study on model scaling. Results indicate that performance gains from scaling consistently transfer to the WOD benchmark as model size increases.

Detection	Midtraining Task		L2 APH Overall
	Roadgraph Pred.	Occupancy Pred.	
✓			75.7
✓	✓		76.3
✓	✓	✓	76.6

Table 7. Ablation study on mid-training tasks using STELLAR-96M model. Adding extra tasks during mid-training leads to improved 3D detection performance in WOD.

#### 7.2.2. MODEL SCALING

Table 6 presents fine-tuning results on WOD following pre-training across varying model sizes. To isolate the effects of pre-training scaling, we omit the mid-training stage in these experiments. Results demonstrate that scaling benefits consistently transfer to WOD performance as model size increases. Fig. 1 further illustrates this trend by plotting performance as a function of FLOPs.

#### 7.2.3. MID-TRAINING TASKS

We investigate the benefit of introducing additional tasks and supervisions in the mid-training stage, as described in Sec. 5. This stage, which uses high-quality human-annotated data, is added on top of a pre-training phase that uses a detection-only task on our vast auto-labeled dataset. The results are presented in Tab. 7. We show that adding extra supervision tasks during mid-training, such as roadgraph prediction and occupancy prediction, progressively improves L2 APH on the WOD validation set.

#### 7.2.4. MULTI-MODAL INPUTS

Tab. 8 presents 3D detection performance on the WOD validation set as we incrementally add input modalities (LiDAR, camera, and surfel map prior) during fine-tuning on WOD. The results indicate that each additional modality improves overall performance, as measured by L2 APH.

#### 7.2.5. TEMPORAL CONTEXT

Tab. 9 details the impact of increasing the temporal context when fine-tuning a LiDAR-only model on the WOD validation set. The results demonstrate a consistent improvement in performance across all object categories as the con-

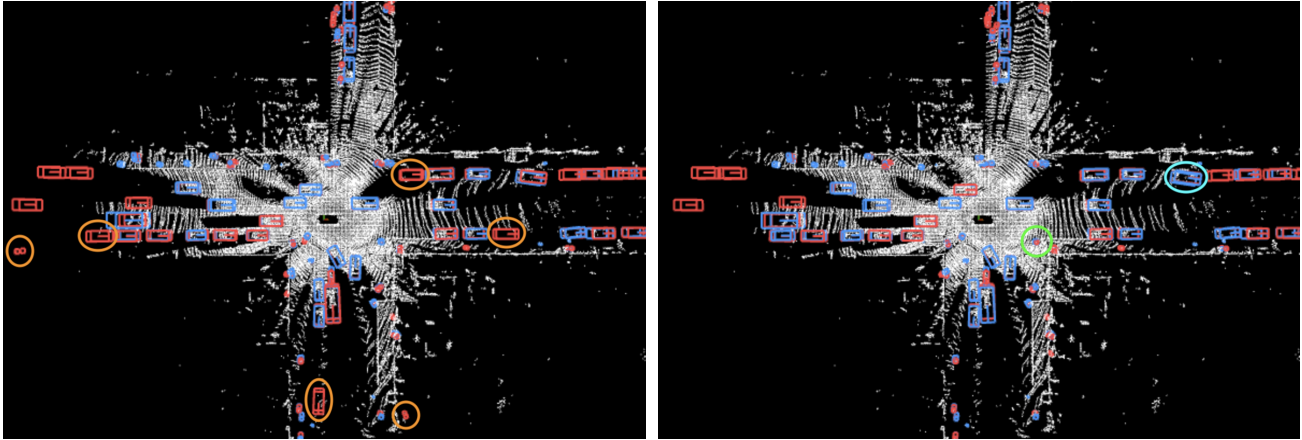


Figure 6. Qualitative comparison of the STELLAR-96M (left) and STELLAR-483M (right) models, pre-trained on the full dataset and finetuned on the WOD validation set. Ground truth boxes are shown in blue, and predictions (confidence > 0.2) are in red. Compared to the smaller model, the larger model (right) demonstrates superior performance: it successfully detects a pedestrian at the crosswalk (green), yields more accurate bounding box prediction (cyan), and produces fewer false positives (orange).

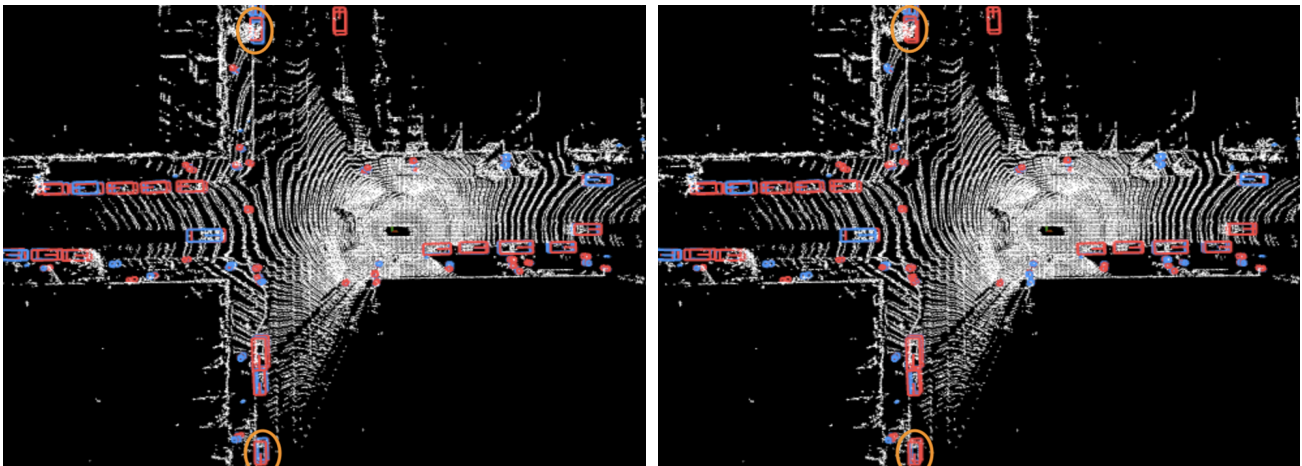


Figure 7. Qualitative comparison of the STELLAR-483M model pre-trained on the 12.8M dataset (left) vs. the full dataset (right) and finetuned on WOD. Ground truth boxes are shown in blue, and predictions (confidence > 0.2) are in red. The model trained on more examples exhibits better quality detections, especially in long range (highlighted in orange).

Input Modality			L2 APH
LiDAR	Camera	Surfel	Overall
✓			74.9
✓	✓		75.7
✓	✓	✓	76.1

Table 8. Ablation study on input modalities using STELLAR-96M model. Adding camera and surfel inputs leads to improved 3D detection performance in WOD.

Number of Input Frames	L2 APH			
	Overall	Vehicle	Pedestrian	Cyclist
2	73.3	75.9	69.2	74.7
4	75.7	78.8	71.7	76.5
6	76.1	80.0	72.1	76.3
8	76.4	80.7	72.3	76.1

Table 9. Ablation study on the number of input frames using the STELLAR-96M model. Finetuning performance consistently improves up to 4 input frames, aligning with the temporal context used during the pre-training and mid-training stages. Beyond 4 frames, we observe a divergence in performance across different object categories.

text window expands up to four frames, which aligns with the temporal context used during the pre-training and mid-training stages. Beyond this point, the overall improvements begin to plateau. Notably, we observe a divergence: performance for vehicle and pedestrian types improves slightly, while cyclist detection performance degrades.

To balance between computational efficiency and performance, we select a temporal context of four frames for STELLAR.

### 7.2.6. MODEL DISTILLATION

During distillation, we employ the best STELLAR model as teacher, and the student model is the smallest 25M variant. Using our mid-training dataset, the student undergoes a two-stage training process: 160,000 steps of distillation using teacher-generated targets, followed by 40,000 steps of fine-tuning on human-annotated labels. This distilled student achieves a 4.7% improvement in overall L2 APH compared to a baseline trained exclusively on human-annotated labels for the full 200,000 steps.

### 7.3. Qualitative Comparison

We present two pairs of qualitative examples to demonstrate the effectiveness of scaling in terms of model parameters and data sizes. More examples can be found in Appendix E.

#### 7.3.1. MODEL SCALING

Fig. 6 provides a qualitative comparison between a smaller and a larger model pre-trained on full dataset and finetuned on WOD. The larger model demonstrates superior performance: it predicts box locations more accurately (cyan circle), better handles challenging pedestrian objects with few points (green circle), and produces fewer false positives (orange circles).

#### 7.3.2. DATA SCALING

Fig. 7 provides a qualitative comparison of the same STELLAR-483M model pre-trained on small versus large datasets and finetuned on WOD. The model trained on the larger dataset demonstrates better performance, by predicting more accurate box locations in longer range with sparser points. As highlighted by the orange circles, its predictions (red) align better with the groundtruth (blue).

## 8. Conclusion

We present STELLAR, a comprehensive study systematically analyzing the impact of scale on 3D perception for autonomous driving. Our model accepts multi-modality inputs from diverse sensors, including LiDAR, radar, camera, and surfel map prior. These sensor data are jointly processed in BEV space using a sparse window Transformer backbone. By training models with up to 500 million parameters on 50 million driving examples, a total compute budget exceeding 10 ZettaFLOPs, we establish empirical scaling trends that relate performance to data volume, model size, and compute. The resulting model sets a new state-of-the-art on the Waymo Open Dataset by a substantial margin. Our findings provide strong evidence that large-scale training, particularly with multi-modal data and multi-task training, is a pivotal direction for advancing perception model capabilities for autonomous driving.

## References

- Achiam, J., Adler, S., Agarwal, S., Ahmad, L., Akkaya, I., Aleman, F. L., Almeida, D., Altenschmidt, J., Altman, S., Anadkat, S., et al. GPT-4 technical report. *arXiv preprint arXiv:2303.08774*, 2023.
- Agro, B., Sykora, Q., Casas, S., Gilles, T., and Urtasun, R. UnO: Unsupervised occupancy fields for perception and forecasting. In *Proceedings of the IEEE/CVF Conference on Computer Vision and Pattern Recognition*, pp. 14487–14496, 2024.
- Agro, B., Casas, S., Wang, P., Gilles, T., and Urtasun, R. MAD: Memory-augmented detection of 3d objects. In *Proceedings of the Computer Vision and Pattern Recognition Conference*, pp. 1449–1460, 2025.
- Baniodeh, M., Goel, K., Ettinger, S., Fuertes, C., Seff, A., Shen, T., Gulino, C., Yang, C., Jerfel, G., Choe, D., et al. Scaling laws of motion forecasting and planning—a technical report. *arXiv preprint arXiv:2506.08228*, 2025.
- Brown, T., Mann, B., Ryder, N., Subbiah, M., Kaplan, J. D., Dhariwal, P., Neelakantan, A., Shyam, P., Sastry, G., Askell, A., et al. Language models are few-shot learners. *Advances in neural information processing systems*, 33: 1877–1901, 2020.
- Bulatov, Y. Fitting larger networks into memory. Technical report, Tensorflow, Medium, 2018.
- Caesar, H., Bankiti, V., Lang, A. H., Vora, S., Liong, V. E., Xu, Q., Krishnan, A., Pan, Y., Baldan, G., and Beijbom, O. nuscenes: A multimodal dataset for autonomous driving. In *Proceedings of the IEEE/CVF conference on computer vision and pattern recognition*, pp. 11621–11631, 2020.
- Caron, M., Touvron, H., Misra, I., Jégou, H., Mairal, J., Bojanowski, P., and Joulin, A. Emerging properties in self-supervised vision transformers. In *Proceedings of the IEEE/CVF international conference on computer vision*, pp. 9650–9660, 2021.
- Chen, T., Xu, B., Zhang, C., and Guestrin, C. Training deep nets with sublinear memory cost. *arXiv preprint arXiv:1604.06174*, 2016.
- Devlin, J., Chang, M.-W., Lee, K., and Toutanova, K. BERT: Pre-training of deep bidirectional transformers for language understanding. In *Proceedings of Association for Computational Linguistics (ACL)*, pp. 4171–4186, 2019.
- Duan, K., Bai, S., Xie, L., Qi, H., Huang, Q., and Tian, Q. CenterNet: Keypoint triplets for object detection. In *Proceedings of the IEEE/CVF international conference on computer vision*, pp. 6569–6578, 2019.

- Fan, L., Pang, Z., Zhang, T., Wang, Y.-X., Zhao, H., Wang, F., Wang, N., and Zhang, Z. Embracing single stride 3d object detector with sparse transformer. In *Proceedings of the IEEE/CVF conference on computer vision and pattern recognition*, pp. 8458–8468, 2022a.
- Fan, L., Wang, F., Wang, N., and Zhang, Z.-X. Fully sparse 3d object detection. *Advances in Neural Information Processing Systems*, 35:351–363, 2022b.
- Fan, L., Yang, Y., Wang, F., Wang, N., and Zhang, Z. Super sparse 3d object detection. *IEEE Transactions on Pattern Analysis and Machine Intelligence*, 2023.
- Fan, L., Wang, F., Wang, N., and Zhang, Z. FSD v2: Improving fully sparse 3d object detection with virtual voxels. *IEEE Transactions on Pattern Analysis and Machine Intelligence*, 2024.
- Fu, Y., Zou, Y., Xiang, H., Huang, X., Bai, Y., Song, C., Shi, W., Thattai, G., Anguelov, D., Tan, M., and Li, Y. Scene reconstruction as mapping priors for 3d detection. In *Proceedings of the IEEE conference on computer vision and pattern recognition*, 2026.
- Hägele, A., Bakouch, E., Kosson, A., Von Werra, L., Jaggi, M., et al. Scaling laws and compute-optimal training beyond fixed training durations. *Advances in Neural Information Processing Systems*, 37:76232–76264, 2024.
- He, C., Li, R., Zhang, Y., Li, S., and Zhang, L. MSF: Motion-guided sequential fusion for efficient 3d object detection from point cloud sequences. In *Proceedings of the IEEE/CVF Conference on Computer Vision and Pattern Recognition*, pp. 5196–5205, 2023.
- He, K., Zhang, X., Ren, S., and Sun, J. Deep residual learning for image recognition. In *Proceedings of the IEEE conference on computer vision and pattern recognition*, pp. 770–778, 2016.
- He, K., Girshick, R., and Dollár, P. Rethinking imagenet pre-training. In *Proceedings of the IEEE/CVF international conference on computer vision*, pp. 4918–4927, 2019.
- Hess, G., Jaxing, J., Svensson, E., Hagerman, D., Petersson, C., and Svensson, L. Masked autoencoder for self-supervised pre-training on lidar point clouds. In *Proceedings of the IEEE/CVF winter conference on applications of computer vision*, pp. 350–359, 2023.
- Hoffmann, J., Borgeaud, S., Mensch, A., Buchatskaya, E., Cai, T., Rutherford, E., Casas, D. d. L., Hendricks, L. A., Welbl, J., Clark, A., et al. Training compute-optimal large language models. *arXiv preprint arXiv:2203.15556*, 2022.
- Hu, Y., Yang, J., Chen, L., Li, K., Sima, C., Zhu, X., Chai, S., Du, S., Lin, T., Wang, W., et al. Planning-oriented autonomous driving. In *Proceedings of the IEEE/CVF conference on computer vision and pattern recognition*, pp. 17853–17862, 2023.
- Huang, C., Abdelzad, V., Sedwards, S., and Czarnecki, K. Vadet: Multi-frame lidar 3d object detection using variable aggregation. In *2025 IEEE/CVF Winter Conference on Applications of Computer Vision (WACV)*, pp. 711–720. IEEE, 2025a.
- Huang, G., Sun, Y., Liu, Z., Sedra, D., and Weinberger, K. Q. Deep networks with stochastic depth. In *European conference on computer vision*, pp. 646–661. Springer, 2016.
- Huang, J., Huang, G., Zhu, Z., Ye, Y., and Du, D. BEVDet: High-performance multi-camera 3d object detection in bird-eye-view. *arXiv preprint arXiv:2112.11790*, 2021.
- Huang, X., Wolff, E. M., Vernaza, P., Phan-Minh, T., Chen, H., Hayden, D. S., Edmonds, M., Pierce, B., Chen, X., Jacob, P. E., et al. DriveGPT: Scaling autoregressive behavior models for driving. In *International conference on machine learning*. PmlR, 2025b.
- Ibrahim, A., Thérien, B., Gupta, K., Richter, M. L., Anthony, Q., Lesort, T., Belilovsky, E., and Rish, I. Simple and scalable strategies to continually pre-train large language models. *arXiv preprint arXiv:2403.08763*, 2024.
- Kaplan, J., McCandlish, S., Henighan, T., Brown, T. B., Chess, B., Child, R., Gray, S., Radford, A., Wu, J., and Amodei, D. Scaling laws for neural language models. *arXiv preprint arXiv:2001.08361*, 2020.
- Karnchanachari, N., Geromichalos, D., Tan, K. S., Li, N., Eriksen, C., Yaghoubi, S., Mehdipour, N., Bernasconi, G., Fong, W. K., Guo, Y., et al. Towards learning-based planning: The nuplan benchmark for real-world autonomous driving. In *2024 IEEE International Conference on Robotics and Automation (ICRA)*, pp. 629–636. IEEE, 2024.
- Lang, A. H., Vora, S., Caesar, H., Zhou, L., Yang, J., and Beijbom, O. PointPillars: Fast encoders for object detection from point clouds. In *Proceedings of the IEEE/CVF conference on computer vision and pattern recognition*, pp. 12697–12705, 2019.
- Li, X., Ma, T., Hou, Y., Shi, B., Yang, Y., Liu, Y., Wu, X., Chen, Q., Li, Y., Qiao, Y., et al. LoGoNet: Towards accurate 3d object detection with local-to-global cross-modal fusion. In *Proceedings of the IEEE/CVF conference on computer vision and pattern recognition*, pp. 17524–17534, 2023a.

- Li, Y., Qi, C. R., Zhou, Y., Liu, C., and Anguelov, D. Modar: Using motion forecasting for 3d object detection in point cloud sequences. In *Proceedings of the IEEE/CVF Conference on Computer Vision and Pattern Recognition*, pp. 9329–9339, 2023b.
- Li, Z., Wang, W., Li, H., Xie, E., Sima, C., Lu, T., Yu, Q., and Dai, J. BEVFormer: learning bird’s-eye-view representation from lidar-camera via spatiotemporal transformers. *IEEE Transactions on Pattern Analysis and Machine Intelligence*, 2024.
- Liu, Z., Tang, H., Amini, A., Yang, X., Mao, H., Rus, D., and Han, S. Bevfusion: Multi-task multi-sensor fusion with unified bird’s-eye view representation. *ICRA*, 2023.
- Liu, Z., Hou, J., Wang, X., Ye, X., Wang, J., Zhao, H., and Bai, X. LION: Linear group rnn for 3d object detection in point clouds. *Advances in Neural Information Processing Systems*, 37:13601–13626, 2024a.
- Liu, Z., Hou, J., Ye, X., Wang, T., Wang, J., and Bai, X. SEED: A simple and effective 3d detr in point clouds. In *European Conference on Computer Vision*, pp. 110–126. Springer, 2024b.
- Ljungbergh, W., Lilja, A., Ling, A. T., Lindström, C., Verbeke, W., Fu, J., Petersson, C., Hammarstrand, L., Felsberg, M., et al. GASP: Unifying geometric and semantic self-supervised pre-training for autonomous driving. *arXiv preprint arXiv:2503.15672*, 2025.
- Luo, W., Yang, B., and Urtasun, R. Fast and furious: Real time end-to-end 3d detection, tracking and motion forecasting with a single convolutional net. In *Proceedings of the IEEE conference on Computer Vision and Pattern Recognition*, pp. 3569–3577, 2018.
- Petty, J., Steenkiste, S., Dasgupta, I., Sha, F., Garrette, D., and Linzen, T. The impact of depth on compositional generalization in transformer language models. In *Proceedings of Association for Computational Linguistics (ACL)*, pp. 7239–7252, 2024.
- Pfister, H., Zwicker, M., Van Baar, J., and Gross, M. Surfels: Surface elements as rendering primitives. In *Proceedings of the 27th annual conference on Computer graphics and interactive techniques*, pp. 335–342, 2000.
- Phillion, J. and Fidler, S. Lift, splat, shoot: Encoding images from arbitrary camera rigs by implicitly unprojecting to 3d. In *European conference on computer vision*, pp. 194–210. Springer, 2020.
- Qi, C. R., Su, H., Mo, K., and Guibas, L. J. PointNet: Deep learning on point sets for 3d classification and segmentation. In *Proceedings of the IEEE conference on computer vision and pattern recognition*, pp. 652–660, 2017.
- Radford, A., Narasimhan, K., Salimans, T., Sutskever, I., et al. Improving language understanding by generative pre-training. *OpenAI blog*, 2018.
- Radford, A., Kim, J. W., Hallacy, C., Ramesh, A., Goh, G., Agarwal, S., Sastry, G., Askell, A., Mishkin, P., Clark, J., et al. Learning transferable visual models from natural language supervision. In *International conference on machine learning*, pp. 8748–8763. PmlR, 2021.
- Schreier, T., Renz, K., Geiger, A., and Chitta, K. On off-line evaluation of 3d object detection for autonomous driving. In *Proceedings of the IEEE/CVF International Conference on Computer Vision*, pp. 4084–4089, 2023.
- Sun, P., Kretschmar, H., Dotiwalla, X., Chouard, A., Patnaik, V., Tsui, P., Guo, J., Zhou, Y., Chai, Y., Caine, B., et al. Scalability in perception for autonomous driving: Waymo open dataset. In *Proceedings of the IEEE/CVF conference on computer vision and pattern recognition*, pp. 2446–2454, 2020.
- Sun, P., Tan, M., Wang, W., Liu, C., Xia, F., Leng, Z., and Anguelov, D. SWFormer: Sparse window transformer for 3d object detection in point clouds. In *European Conference on computer vision*, pp. 426–442. Springer, 2022.
- Sun, T., Zhang, Z., Tan, X., Peng, Y., Qu, Y., and Xie, Y. Uni-to-multi modal knowledge distillation for bidirectional lidar-camera semantic segmentation. *IEEE Transactions on Pattern Analysis and Machine Intelligence*, 2024.
- Team, G., Anil, R., Borgeaud, S., Alayrac, J.-B., Yu, J., Soricut, R., Schalkwyk, J., Dai, A. M., Hauth, A., Millican, K., et al. Gemini: a family of highly capable multimodal models. *arXiv preprint arXiv:2312.11805*, 2023.
- Tian, X., Jiang, T., Yun, L., Mao, Y., Yang, H., Wang, Y., Wang, Y., and Zhao, H. Occ3D: A large-scale 3d occupancy prediction benchmark for autonomous driving. *Advances in Neural Information Processing Systems*, 36: 64318–64330, 2023.
- Wei, Y., Zhao, L., Zheng, W., Zhu, Z., Zhou, J., and Lu, J. Surroundocc: Multi-camera 3d occupancy prediction for autonomous driving. In *Proceedings of the IEEE/CVF International Conference on Computer Vision*, pp. 21729–21740, 2023.
- Wilson, B., Qi, W., Agarwal, T., Lambert, J., Singh, J., Khandelwal, S., Pan, B., Kumar, R., Hartnett, A., Pontes, J. K., et al. Argoverse 2: Next generation datasets for self-driving perception and forecasting. *arXiv preprint arXiv:2301.00493*, 2023.

- Wozniak, M. K., Govindarajan, H., Klingner, M., Maurice, C., Kiran, B. R., and Yogamani, S. S3PT: Scene semantics and structure guided clustering to boost self-supervised pre-training for autonomous driving. In *2025 IEEE/CVF Winter Conference on Applications of Computer Vision (WACV)*, pp. 1660–1670. IEEE, 2025.
- Wu, X., Jiang, L., Wang, P.-S., Liu, Z., Liu, X., Qiao, Y., Ouyang, W., He, T., and Zhao, H. Point Transformer V3: Simpler faster stronger. In *Proceedings of the IEEE/CVF conference on computer vision and pattern recognition*, pp. 4840–4851, 2024.
- Yaak, T. LeRobot goes to driving school: World’s largest open-source self-driving dataset. <https://www.huggingface.com/blog/lerobot-goes-to-driving-school>, 2025.
- Yang, H., Zhang, S., Huang, D., Wu, X., Zhu, H., He, T., Tang, S., Zhao, H., Qiu, Q., Lin, B., et al. UniPAD: A universal pre-training paradigm for autonomous driving. In *Proceedings of the IEEE/CVF conference on computer vision and pattern recognition*, pp. 15238–15250, 2024.
- Yang, Z., Chai, Y., Anguelov, D., Zhou, Y., Sun, P., Erhan, D., Rafferty, S., and Kretschmar, H. SurfGAN: Synthesizing realistic sensor data for autonomous driving. In *Proceedings of the IEEE/CVF Conference on Computer Vision and Pattern Recognition*, pp. 11118–11127, 2020.
- Yin, T., Zhou, X., and Krahenbuhl, P. Center-based 3d object detection and tracking. In *Proceedings of the IEEE/CVF conference on computer vision and pattern recognition*, pp. 11784–11793, 2021.
- You, Y., Li, J., Reddi, S., Hseu, J., Kumar, S., Bhojanapalli, S., Song, X., Demmel, J., Keutzer, K., and Hsieh, C.-J. Large batch optimization for deep learning: Training bert in 76 minutes. *arXiv preprint arXiv:1904.00962*, 2019.
- Zhang, G., Junnan, C., Gao, G., Li, J., and Hu, X. HEDNet: A hierarchical encoder-decoder network for 3d object detection in point clouds. *Advances in Neural Information Processing Systems*, 36:53076–53089, 2023.
- Zhang, G., Chen, J., Gao, G., Li, J., Liu, S., and Hu, X. SAFDNet: A simple and effective network for fully sparse 3d object detection. In *Proceedings of the IEEE/CVF Conference on Computer Vision and Pattern Recognition*, pp. 14477–14486, 2024.
- Zhou, Y. and Tuzel, O. VoxelNet: End-to-end learning for point cloud based 3d object detection. In *Proceedings of the IEEE conference on computer vision and pattern recognition*, pp. 4490–4499, 2018.
- Zhou, Y., Sun, P., Zhang, Y., Anguelov, D., Gao, J., Ouyang, T., Guo, J., Ngiam, J., and Vasudevan, V. End-to-end multi-view fusion for 3d object detection in lidar point clouds. In *Conference on Robot Learning*, pp. 923–932. PMLR, 2020.
- Zhou, Z., Zhao, X., Wang, Y., Wang, P., and Foroosh, H. CenterFormer: Center-based transformer for 3d object detection. In *European Conference on Computer Vision*, pp. 496–513. Springer, 2022.

### A. Additional Model Details

Our backbone is based on the SWFormer architecture (Sun et al., 2022), which processes input features through a 5-scale sequence of Transformer blocks. These blocks efficiently generate feature maps at different granularities, using relative strides of [1, 2, 4, 16, 32] across the sequence.

We initialize our smallest model using the implementation details reported in SWFormer: a channel size (hidden dimension) of 128, an MLP ratio (feed-forward ratio) of 2, a head size of 8, and layer counts of [2, 3, 2, 3, 2] for the five scales, respectively. From this baseline, we progressively scale the model size up to approximately 500 million parameters, as detailed in Tab. 2.

The occupancy prediction task classifies voxels into a finite set of semantic labels. The task head is composed of a  $3 \times 3$  convolutional layer and an MLP that processes backbone features to output a single class per voxel. The roadgraph prediction task head follows a similar design. We render map elements, such as lanes and road boundaries, in bird’s-eye view (BEV) to define per-voxel supervision targets. We adopt simple, lightweight heads for both tasks; this design facilitates robust multi-task mid-training and effectively encourages the backbone to generalize across distinct perception domains.

### B. Additional Training Details

Tab. 10 provides a detailed comparison of our three-stage training recipe. We select inputs and tasks for each stage based on the scale and quality of the training dataset.

### C. Quantitative Comparison on Rare Classes

Tab. 6 demonstrates the significant improvement in L2 APH on the WOD dataset achieved by scaling model parameters. Given that the object classes in WOD are primarily focused on common classes, we extended our evaluation to a set of challenging object classes (e.g., stroller, animal, and traffic cone) using an internal dataset. The results confirm the effectiveness of scaling on these difficult categories: the mAP improved by 5.5% from STELLAR-25M to STELLAR-96M, and by 7.9% from STELLAR-96M to STELLAR-483M. Furthermore, in a more rigorous benchmark focused on rare and hard cases, STELLAR-483M achieved a 25% error rate reduction over STELLAR-96M across various AP and recall metrics. These findings collectively suggest that the benefits of scaling extend beyond common object types, generalizing to more infrequent and challenging rare classes.

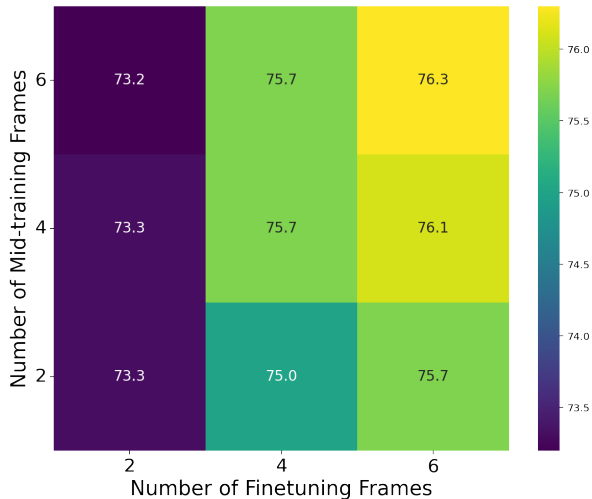


Figure 8. Temporal context ablation across mid-training and finetuning. The results reveal that Overall L2 APH consistently improves as the number of finetuning frames increases, regardless of the mid-training frames at (2, 4, 6). Furthermore, longer context in mid-training offers limited benefit when finetuning uses fewer frames.

### D. Additional Ablation Studies

In this section, we provide additional ablation studies on temporal context during mid-training and finetuning, as well as perception range during training and inference.

#### D.1. Temporal Context during Mid-training

To assess the impact of temporal context length during mid-training, we extend the ablation study presented in Sec. 7.2.5, which fixed the mid-training temporal frames to 4. Fig. 8 summarizes the Overall L2 APH results across different combinations of mid-training and finetuning temporal frames.

We find that the Overall L2 APH consistently improves as the number of finetuning frames increases, irrespective of the mid-training configuration. While the peak performance is achieved using 6 temporal frames, we observe that longer context in mid-training offers limited benefit when finetuning uses fewer frames. For example, mid-training with 6 frames yields no performance gain over 4 frames when the model is subsequently finetuned using only 4 frames. This behavior is further supported by the 2-frame finetuning results, which exhibit highly similar performance regardless of the number of frames used during mid-training.

#### D.2. Perception Range

To validate the scalability of our model with respect to perception range during inference, we evaluated the STELLAR-96M model, originally trained with the WOD range setting

## STELLAR: Scaling 3D Perception Large Models for Autonomous Driving

Stage	Dataset	LiDAR	Inputs			Detection	Tasks		Learning Rate
			Radar	Camera	Surfel		Roadgraph	Occupancy	
Pre-training	Internal full	✓ (4 frames)	✓	✓		✓			Constant
Mid-training	Internal human-annotated	✓ (4 frames)	✓	✓	✓	✓	✓	✓	Cosine decay
Finetuning	WOD	✓ (4 frames)		✓	✓	✓			Cosine decay

Table 10. The STELLAR training recipe consists of three sequential stages: pre-training a detection model on the large-scale internal dataset; mid-training on a human-annotated dataset using a multi-task objective and all input features; and finally, finetuning a detection-only model on WOD. The surfel input is derived from LiDAR and camera inputs, as described in Sec. 3.

Perception Range (Inference)	Overall L2 APH	
	Range [0, 30)	Range [30, 50)
75	86.5	74.7
50	86.8	74.8
30	86.8	0.0

Table 11. Ablation study on perception range during inference, by training the STELLAR-96M model at 75-meter range and reducing the range during inference. The results show that performance is comparable within the available detection range when the inference distance is reduced, validating the model’s robustness to varying ranges.

Perception Range (Training)	Overall L2 APH	
	Range [0, 30)	Range [30, 50)
30	86.7	0.0
50	86.7	74.3
75	86.5	74.7

Table 12. Ablation study on perception range, by training the STELLAR-96M model at different ranges and evaluating the model performance at two ranges. The results show that increasing the range during training does not sacrifice performance in smaller ranges.

at 75 meters, by modifying the inference range to smaller values. The results, reported in Tab. 11, demonstrate that performance remains comparable within the available detection range when the inference distance is reduced. When the detection range is truncated to 30 meters, the Overall L2 APH metric for the [30, 50) meter range is no longer applicable, as expected.

We further investigate the effect of varying the perception range during training and evaluate the resulting detection performance at two different ranges. The results in Tab. 12 indicate that increasing the perception range during training does not sacrifice performance in smaller ranges.

These two ablations, conducted during both inference and training, collectively validate that our model is robust and scalable across different perception range settings.

### E. Additional Qualitative Examples

We present additional qualitative comparisons from model scaling and data scaling as follows.

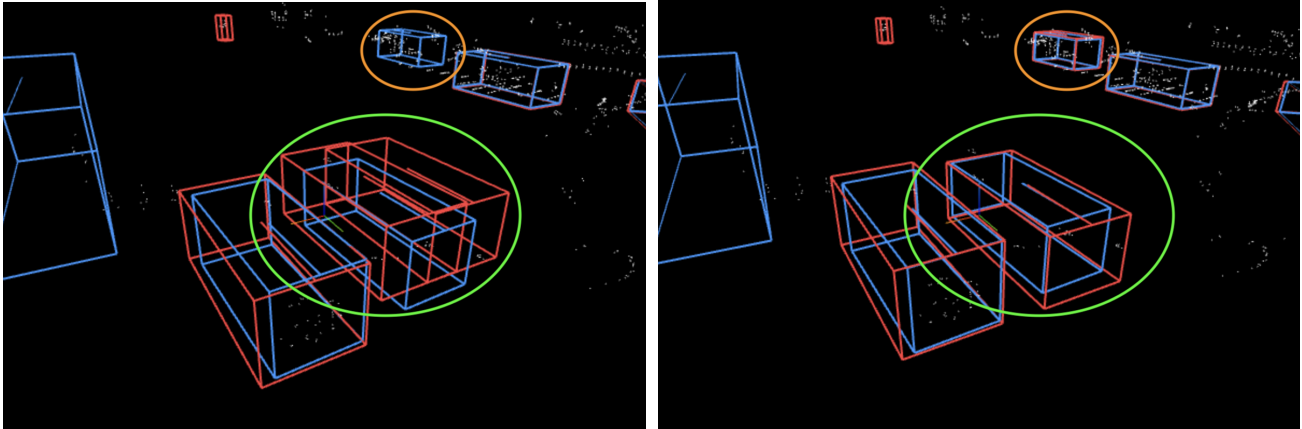
#### E.1. Model Scaling

Fig. 9 presents additional qualitative comparisons between the STELLAR-96M and STELLAR-483M models. Con-

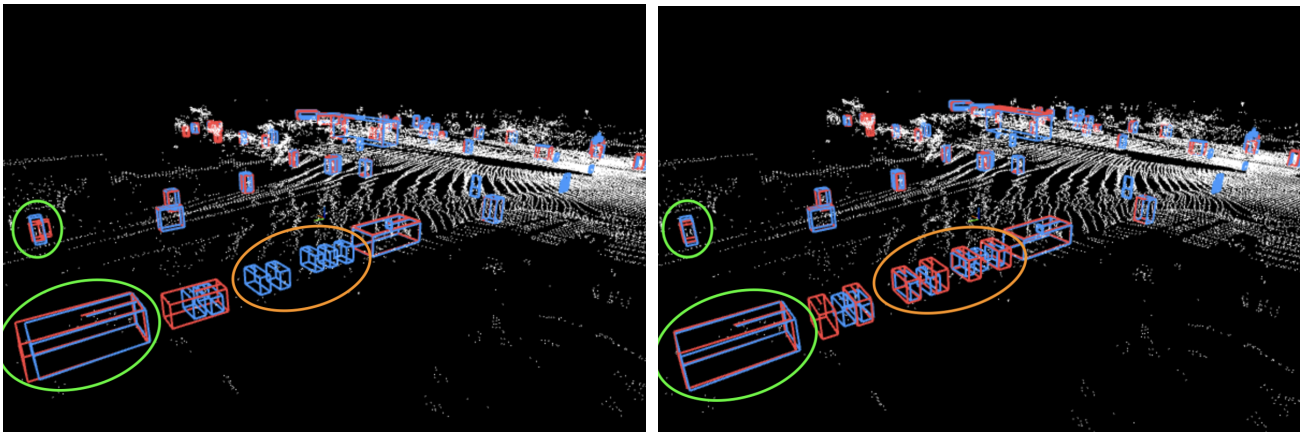
sistent with the observations in Sec. 7.3.1, the larger model demonstrates better performance. Specifically, it achieves higher recall and generates bounding boxes with more accurate location and size in challenging scenarios, including those with sparse points, crowded scenes, and large objects.

#### E.2. Data Scaling

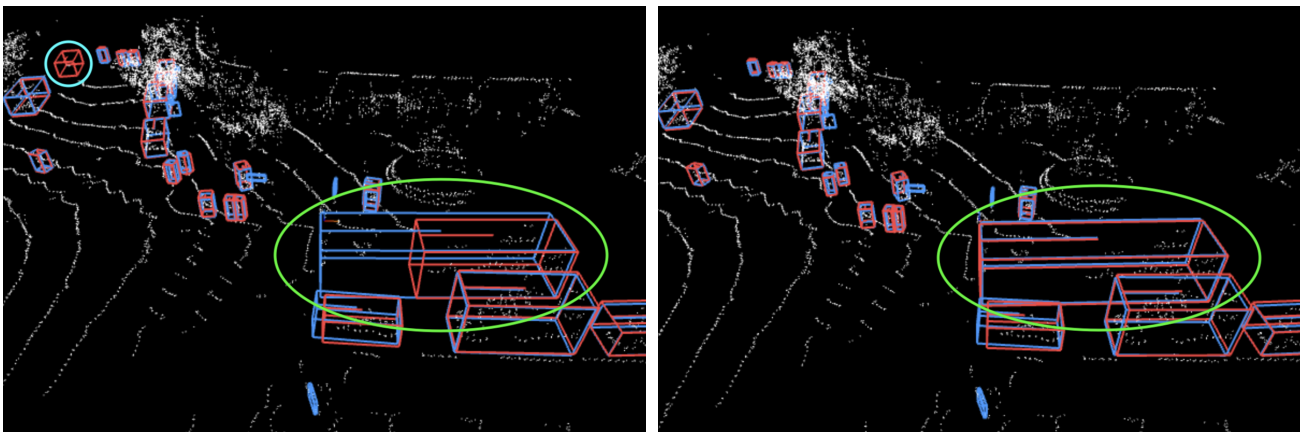
Fig. 10 provides additional qualitative comparisons between two instances of the STELLAR-483M model: one trained on a smaller dataset and the other on the full dataset. Consistent with the observations in Sec. 7.3.2, the model trained on the larger dataset demonstrates better detection results, particularly in scenarios involving sparse points, partial occlusions, and crowded scenes. In contrast, the counterpart trained on the smaller dataset exhibits a higher rate of false positives and less accurate detections.



(a) Detection with sparse points.

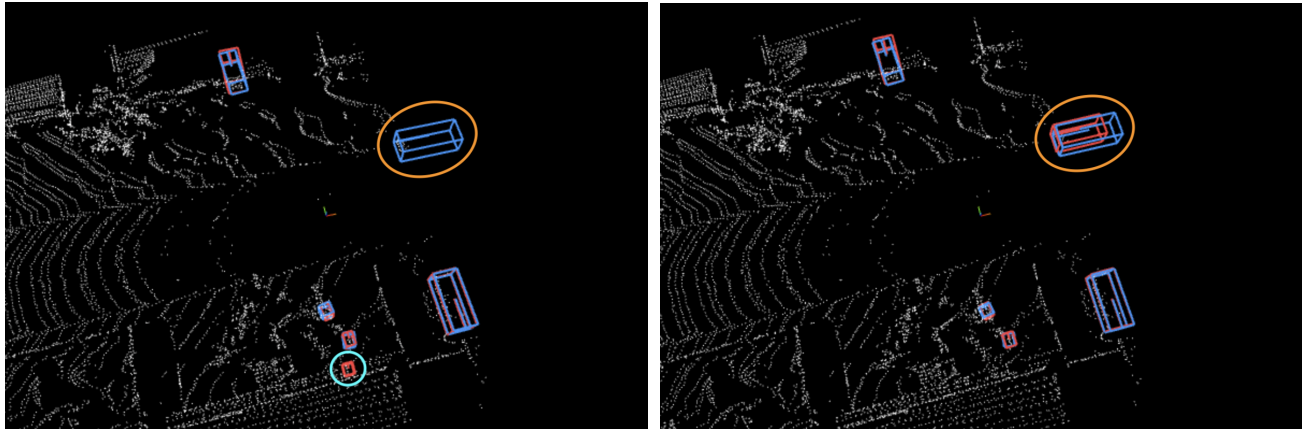


(b) Crowded scene detection.

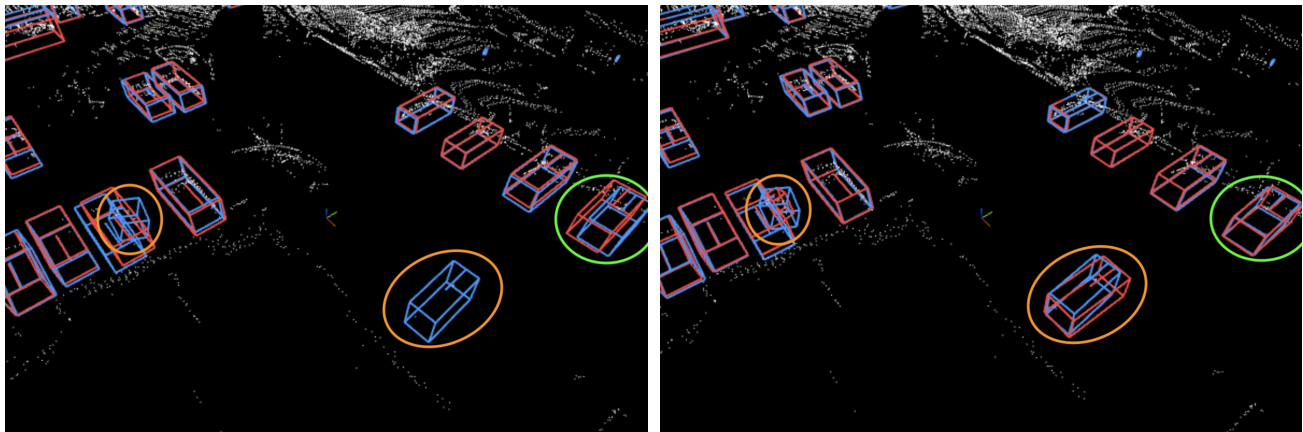


(c) Large object detection.

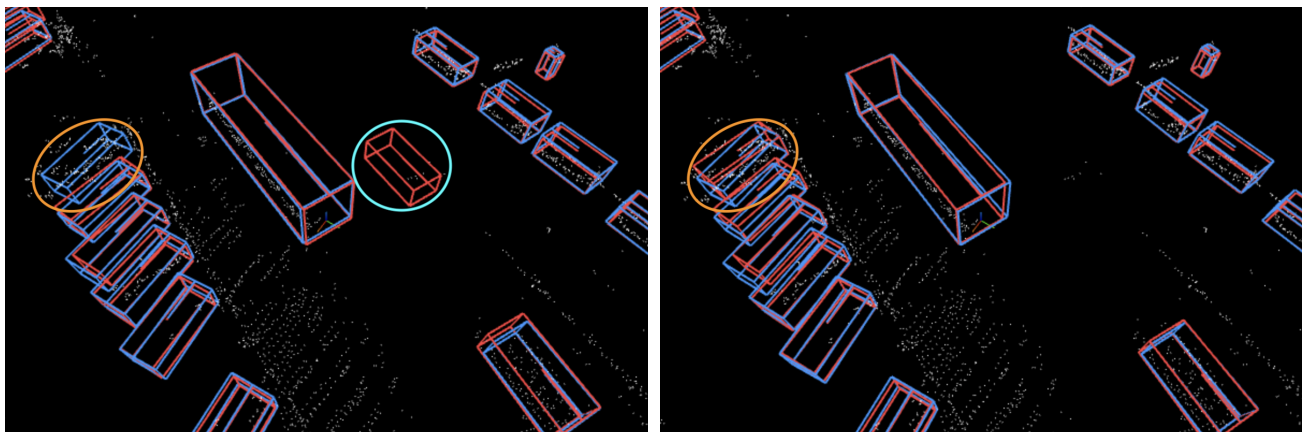
Figure 9. Qualitative comparison of the STELLAR-96M (left column) and STELLAR-483M (right column) models, pre-trained on the full internal dataset and finetuned on WOD. Ground truth boxes are shown in blue, and predictions (confidence  $> 0.2$ ) are in red. In all three examples, the larger model demonstrates superior performance, achieving higher recall (orange) and predicting more accurate location and size (green), in challenging scenarios involving sparse points, crowded scene, and large objects. In contrast, the smaller model exhibits missed detections (orange), inaccurate predictions (green), and false positives (cyan).



(a) Detection with sparse points.



(b) Detection with partial occlusions.



(c) Crowded scene detection.

Figure 10. Qualitative comparison of the STELLAR-483M model pre-trained on the 12.8M dataset (left) vs. the full dataset (right) and finetuned on WOD. Ground truth boxes are shown in blue, and predictions (confidence  $> 0.2$ ) are in red. The model trained on more examples achieves higher recall (orange) and more accurate location (green) in challenging scenarios, involving sparse points, partial occlusions, and crowded scene. In contrast, the smaller model exhibits missed detections (orange), inaccurate predictions (green), and false positives (cyan).